

TURBULENT PIPE FLOW THROUGH A 90° BEND

Leo H. O. Hellström, Metodi B. Zlatinov, Alexander J. Smits

Department of Mechanical and Aerospace Engineering

Princeton University

Princeton, New Jersey 08544, USA

lhellstr@princeton.edu

and Guongjun Cao

CARDC, P. O. Box 211 Mianyang

Sichuan 621000, P. R. China

ABSTRACT

Stereoscopic PIV is used to investigate the structure of fully developed turbulent pipe-flow through a 90° bend. The results show that Dean motions downstream of the bend are very weak in the mean, and time resolved stereoscopic PIV demonstrates that the Dean motions co-exist with large scale swirling motions that switch sign and do not contribute to the mean. Snapshot POD analysis of the flow field reveals that the structures found upstream of the bend persist after the bend and survive the strong secondary motions induced by the pipe curvature. In particular, the Very Large Scale Motions (VLSM) are no longer the most energetic mode in the flow, but they are still the most energetic structure in terms of the streamwise fluctuations.

INTRODUCTION

Turbulent flow in pipe bends is of great practical interest due to the associated pressure losses and the distortion of the velocity profile. Bends tend to introduce secondary flows that lead to scour, and non-uniform heat transfer (Berger et al. 1983). Much research has been done in the area of secondary flows, as it is a phenomena related to many fluid problems, including flow through heat exchangers, industrial plant piping systems, scouring and river meandering.

Early studies showed that secondary vortices in the streamwise direction downstream of the bend (Harlock 1955), the so-called Dean motions (Dean 1928). The strength of the secondary motions is often described using the Dean number, which is the ratio of the square root of the product of the inertia and centrifugal forces to the viscous force. That is,

$$De = \left(\frac{D}{2R_c} \right)^{1/2} \frac{\bar{U}D}{\nu}$$

where D is the pipe diameter, R_c is the radius of curvature, \bar{U} is the area-averaged or bulk velocity, and ν is the fluid kinematic viscosity. In the present work, De is equal to the Reynolds number $Re_D = \bar{U}/D\nu$.

The flow at small Dean numbers has been studied widely because of its appearance in, for example, arterial flows (Boiron et al. 2006), but at high Dean numbers corresponding to turbulent flow where most industrial applications are found there is only scattered evidence available. Studies of the secondary flow in pipes with a 90° bend were conducted using hot wire anemometry by Sudo et al. (1998) for Reynolds numbers of up to 6×10^4 , and their measurements revealed secondary flows that persisted 10 diameters downstream of the bend. However, in some cases a high degree of unsteadiness is observed, as in the study by Tunstall and Harvey (1968) at a Reynolds number of about 1.8×10^5 , which may indicate the presence of a single large streamwise vortex that is switching sign.

The purpose of the present contribution paper is to provide high resolution velocity maps of the primary and secondary flow upstream and downstream of a 90° bend, with $R_c/R = 1$ (where R_c is the radius of bend and R the radius of the pipe). The measurements were obtained using stereoscopic Particle Image Velocimetry (SPIV) at Reynolds numbers up to 10^5 . One of the particular areas of interest is the behavior of the turbulent structure, specifically the Very Large Scale Motions (VLSM), where we build on the recent work of Hellström et al. (2011) who investigated the three-dimensional character of the VLSM in fully-developed pipe flow (that is, in the flow upstream of the bend).

EXPERIMENTAL APPARATUS

The flow facility consists of a 7 meter long clear PVC pipe of internal diameter $D = 40$ mm. The movable test section consists of a glass pipe ($n = 1.472$) which may be placed both upstream and downstream of a 90° bend. The test section is surrounded by a Plexiglas ($n = 1.488$) box filled with glycerin ($n = 1.473$) to minimize optical distortion due to refraction through the pipe wall, shown in figure 1. The pipe bend or the test section, depending on the current setup, was located $150D$ downstream of the pipe entrance to assure a fully developed turbulent pipe flow.

Two sets of stereo Particle Image Velocimetry (PIV) data were obtained. The first set was obtained by recording three separate images: one at $\alpha_1 = +45^\circ$ normal to the flow direction, one at $\alpha_2 = -45^\circ$, and one at $\alpha_3 = 0^\circ$, and the data were used to study the mean flow behavior. The PIV images were recorded using a dual-frame camera (Megaplus ES4.0), operating at 15 fps with a resolution of $2K \times 2K$ pixels. A Nd:YAG double pulse laser with 532 nm beams specified at 200 mJ/pulse was used to illuminate the flow. The laser sheet was oriented normal to the flow with a thickness of 2 mm for angles α_1 and α_2 , and in the streamwise direction on the centerline plane with a thickness of 1 mm for α_3 . The time step between the two frames was selected so that the mean displacement of particles was 3-4 pixels.

The images from α_1 and α_2 were mapped from the image plane to the measurement plane using a mapping function calculated using commercial software (DaVis 6.2, LaVision) based on images of a calibration plate. The calibration plate consisted of a grid of evenly spaced markers spaced 1.6 mm apart. The grid was placed at the center of the laser sheet. PIV data were taken at 5 locations, corresponding to 5 and 10D upstream of the bend, and 5, 10 and 15D downstream of the bend. At each location, 5 Reynolds numbers were investigated, from 3×10^4 to 1.5×10^5 .

A double frame, double exposure cross-correlation method was used to evaluate the two-component vector fields from each set of images, using the LaVision software. The vector fields calculated from images taken from α_3 yielded the streamwise and radial components of the velocity at the center of the pipe. The vector fields calculated from images taken at α_1 and α_2 were first mapped (dewarped) from the angled image planes onto the vertical measurement plane using the image calibration. The LaVision software was then used to calculate the coefficients of the mapping function, using a least square method from the coordinates of the observed and actual position of the calibration markers. Sets of 50 images were averaged to obtain the mean field. The corrected and averaged vector fields from both angles are then interpolated onto a common grid of resolution 100×100 , and combined to yield the three-component vector fields in the radial cross-section of the pipe.

The second set of SPIV experiments were designed to capture time-resolved velocity information. Here, the two images corresponding to α_1 and α_2 were combined onto a single image on the camera, as shown in figure 1. The data were acquired using a Redlake MotionXtra HG-LE camera (up to 1200 fps when using a resolution of 1040 by 640 pixels). The water was seeded with 100 μm diameter neutrally buoyant particles. The maximum Reynolds number is limited to 35,000 because at higher velocities the particles begin to leave the 1.5mm thick laser sheet during the minimum image pair time interval.

In every exposure, the camera records two separate images, each comprising an approximately 45° view of the test section interrogation plane. After each image pair has been separately processed using standard PIV software, the particle displacement fields are mapped into a circular shape using a fourth-order polynomial. The two displacement fields are then fitted onto a common, denser grid using a triangle-based cubic interpolation method. Each data point has one displacement component from both camera views and can then be recon-

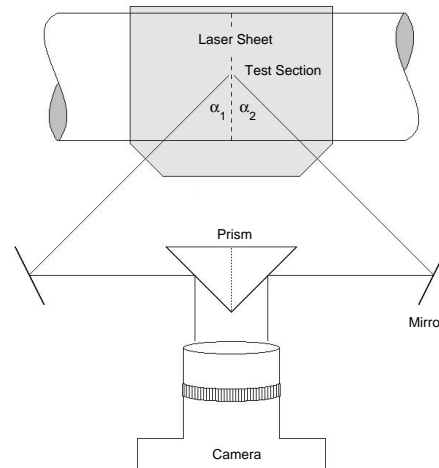


Figure 1. Optical setup for the single-camera SPIV system.

structed into a three component displacement field according to:

$$\Delta x = \frac{\Delta x_2}{\cos \alpha_2} \left(1 - \frac{\cos \alpha_1 \sin \alpha_2}{\sin(\alpha_1 + \alpha_2)} \right) - \frac{\Delta x_1}{\cos \alpha_1} \left(\frac{\cos \alpha_1 \sin \alpha_2}{\sin(\alpha_1 + \alpha_2)} \right) \quad (1)$$

$$\Delta y = \frac{\Delta y_1 + \Delta y_2}{2} \quad (2)$$

$$\Delta z = \frac{\Delta x_2}{\cos \alpha_2} \left(\frac{\cos \alpha_1 \cos \alpha_2}{\sin(\alpha_1 + \alpha_2)} \right) + \frac{\Delta x_1}{\cos \alpha_1} \left(\frac{\cos \alpha_1 \cos \alpha_2}{\sin(\alpha_1 + \alpha_2)} \right) \quad (3)$$

where indices 1 and 2 represents the left and right viewing angles, respectively. Here, Δx , Δy , and Δz are the streamwise, vertical, and horizontal displacement components, respectively. The velocity components in a Cartesian coordinate system are then found by dividing the displacement components by the time delay between successive images. Also, Δx_1 and Δx_2 are the horizontal displacements calculated from the image-halves, while Δy_1 and Δy_2 are the corresponding vertical displacements. The general approach is based on the methodology presented by van Doorne et al. (2007), modified to allow for arbitrary values of α_1 and α_2 . The current experimental setup allows for a data resolution of about 2.15 vectors per mm^2 . The vectors near the wall (for $1 - r/R < 0.1$ where r is the distance from the centerline) have been discarded due to insufficient resolution and reflection problems.

MEAN FLOW RESULTS

The streamwise mean velocity distributions at different distances downstream of the bend are shown in figure 2. The mean velocity profiles, when integrated across the pipe cross-section, agreed with the bulk velocity as measured using a

flowmeter to within 3%, giving some confidence in the accuracy of the data. We see a significant shift of the peak velocity toward the outer part of the bend for downstream distances up to $20D$, but by $50D$ the velocity profile has almost recovered to that seen upstream of the bend. Just downstream of the bend the velocity profiles also a more uniform distribution over at least 60% of the pipe, indicating that a high degree of large-scale mixing takes place within the bend. The profiles were found to be almost independent of Reynolds numbers over the range of investigation ($30 \times 10^3 \leq Re_D \leq 150 \times 10^3$).

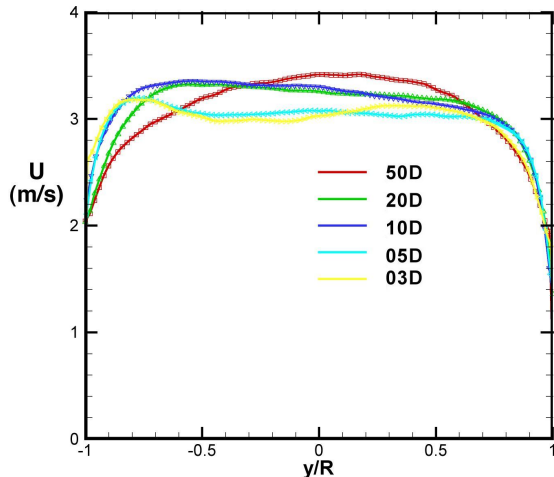


Figure 2. Streamwise mean velocity normalized by bulk velocity, $Re_D = 120,000$. The inside of the bend is at $y/R = 1$.

The mean velocity distributions measured well upstream of the bend in the cross-sectional plane are compared with the values obtained at the first station downstream of the bend ($x = 5.3D$) in figure 3. Again, we see a significant shift of the peak velocity toward the outer part of the bend. The mean velocity is not only shifted towards the outer part of the bend but also flattened out along the outer bend surface for the entire outer half of the plane.

TIME-RESOLVED RESULTS

Tunstall & Harvey (1968) first noticed that for large Dean numbers, the Dean motion is replaced by an unsteady motion consisting of a single swirl oscillating in the clockwise and counterclockwise directions. Their observations were based on flow visualizations and the oscillating frequency was believed to be random. These oscillations can be further investigated using the time-resolved SPIV data at the location $5.3D$ downstream of the bend.

An auto-correlation was performed on the tangential velocity component u_θ to reveal the oscillating behavior. The correlation was performed in the center of one of the cells separated by the symmetry plane. Figure 4 shows a highly oscillating trend and by choosing a velocity pair with a temporal shift corresponding to either a negative or positive correlation, we can visualize the corresponding flow structure.

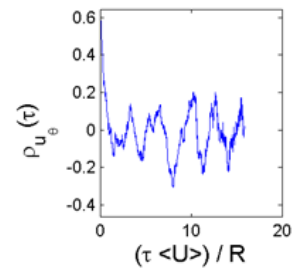


Figure 4. Auto-correlation of the tangential velocity, taken in the center of one of the cells separated by the symmetry line.

For a typical negative correlation, figure 5 shows the contours of the tangential velocity in a cross-sectional plane for time t and $t + \tau$. It can be seen that the left figure shows the presence of a Dean motion whereas the right figure shows a counterclockwise, rotating motion. Similar results are shown for the positive correlation in figure 6, which shows two counterclockwise rotating swirls, although at other times the Dean motion may be present with a clockwise rotating swirl. These observations supports the observations made by Tunstall & Harvey (1968) where the flow downstream of the bend was observed to consist essentially of two counter rotating swirls on the scale of the pipe diameter, but what they did not observe, perhaps because of the limitations on their experiment, was the intermittent appearance of the Dean motions.

Figure 7 shows contour plots of the streamwise component of the vorticity in a cross-sectional plane. The figure to the left displays the mean vorticity, and the one on the right shows a particular realization of the instantaneous vorticity. The most important feature of these two figures is the change of scale: the figure on the right shows contour levels that are a factor of 10 higher than the one on the left. It can be seen that the Dean motion is present in the mean vorticity plot, but it is a relatively weak motion that is almost completely hidden in the much higher levels of instantaneous vorticity.

VERY LARGE SCALE MOTIONS

Recent studies in turbulent wall-bounded flows have revealed the presence of Very Large Scale Motions (VLSM), which are very long, meandering features consisting of narrow regions of low streamwise momentum fluid, flanked by regions of higher momentum fluid. Measurements in channels and pipes have found VLSM as long as 30 times the channel half-height h or pipe radius R (Monty et al. 2007), and for internal geometries the VLSM are found to persist well into the outer layer (Bailey et al. 2010). Balakumar et al. (2007) found that 40-65% of the kinetic energy and 30-50% of the Reynolds shear stress is accounted for in these long modes with streamwise wavelengths greater than $3R$.

Hellström et al. (2011) reported time-resolved stereoscopic PIV measurements of the structure of the VLSM in fully developed turbulent pipe flow in the same apparatus used here but upstream of the bend. The motions were visualized using snapshot POD. It was shown that the structures can be reconstructed using a small number of the most energetic modes, and the results give strong support for the hypothesis

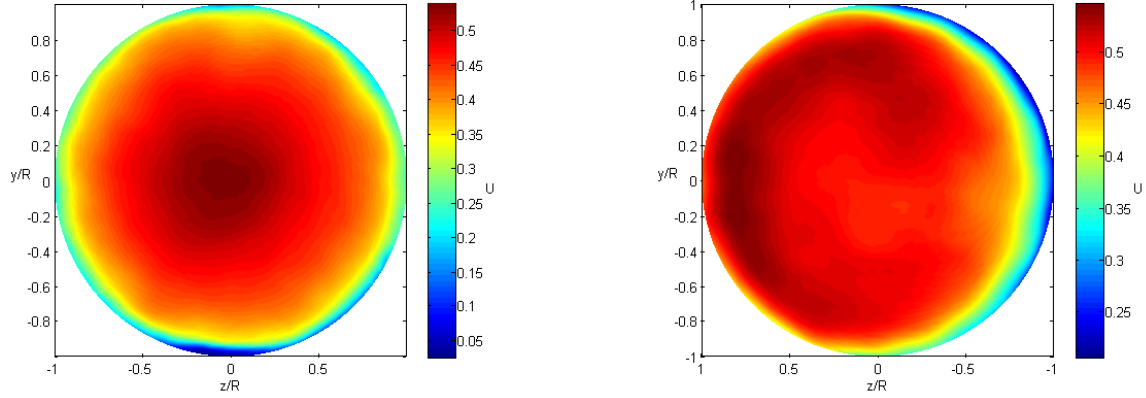


Figure 3. Streamwise velocity contours, $Re_D = 18,000$. The cross-sectional plane. Left: $x = 15D$ upstream of bend. Right: $x = 5D$ downstream of bend.

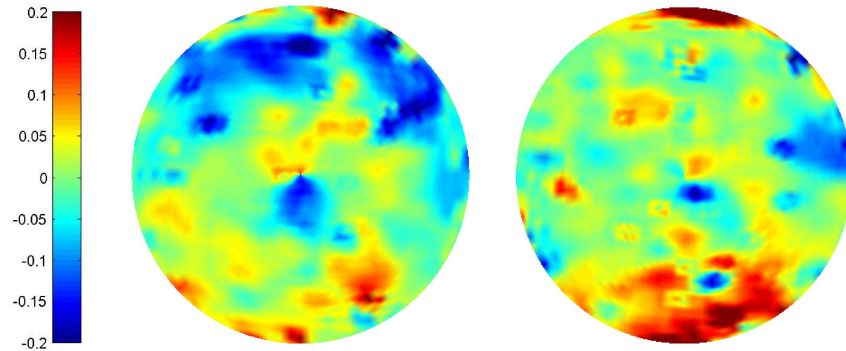


Figure 5. Negative correlation contours, $5.3D$ downstream of the bend, $Re_D = 18,000$. Left: correlation on $u_\theta(t)$. Right: correlation on $u_\theta(t + \tau)$.

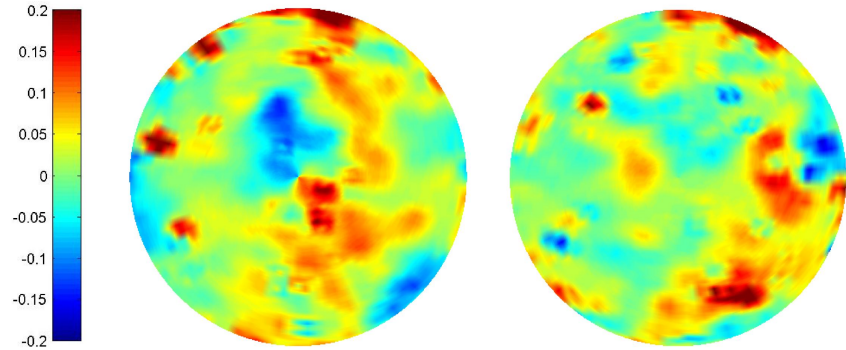


Figure 6. Positive correlation contours, $5.3D$ downstream of the bend, $Re_D = 18,000$. Left: correlation on $u_\theta(t)$. Right: correlation on $u_\theta(t + \tau)$.

proposed by McKeon and Sharma (2010) that selective linear mechanisms may help to explain the origin of the VLSMs. The structures are seen to be highly three-dimensional, meandering azimuthally and radially, and they were seen to occasionally extend from the near-wall region almost to the centerline of the pipe.

Here, we use similar techniques to examine the behavior of the VLSM downstream of the bend. Figure 8(a) shows the streamwise velocity fluctuations u_x at a wall distance

$y' = 1 - y/R = 0.2$, where Taylor's hypothesis is used to translate the time-resolved data to a streamwise distance for easier visualization. The velocity field is viewed in Cartesian coordinates by unrolling the cylindrical plane. The lengths are scaled with the radius of the pipe and the velocity fluctuations with the friction velocity u_τ , where $u_\tau = \sqrt{\tau_w/\rho}$ and the wall stress τ_w is calculated from the pipe friction relationship given by McKeon et al. (2005). The low momentum regions indicate the presence of the VLSMs. Figure 8(b) and

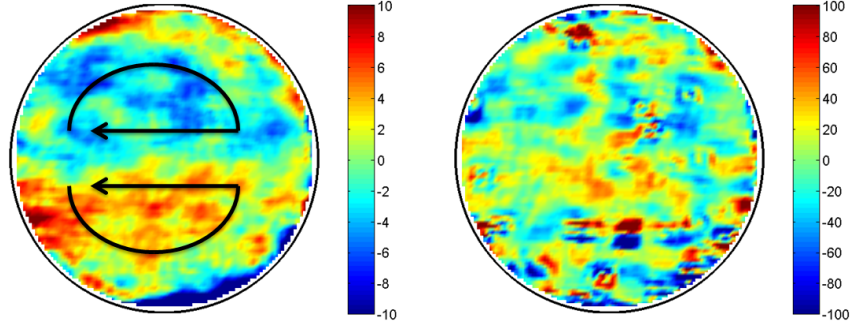


Figure 7. Streamwise vorticity contours, $5.3D$ downstream of the bend, $Re_D = 18,000$. Left: mean vorticity. Right: instantaneous vorticity.

8(c) show the scaled streamwise fluctuations $5D$ downstream of the bend for Reynolds numbers of 12,500 and 16,000, respectively. The contour plots of the downstream velocity fluctuations demonstrate the same low momentum streaks found in the upstream flow. By comparing figure 8(a) with 8(b) and 8(c) it is evident that the general characteristics of the VLSMs are largely unaffected by the pipe curvature, although the structures seem to have increased their streamwise and decreased their azimuthal frequencies, making them appear to be wider and shorter.

It is possible to extract the most energetic structures in the flow by decomposing it into its most energetic modes using snapshot POD, as suggested by Hellström et al. (2011). Figure 9 shows the energy content for the three-component velocity field downstream of the bend. The first mode has about twice the energy of the second and may be recognized as the Dean motion which is induced by the curvature of the pipe. Figure 10 shows the horizontal in-plane velocity component of this mode. It was found that the first five modes are all related to the secondary motions induced by the flow curvature in the bend, in contrast to the case upstream of the bend where the first five modes were all related to the VLSM.

The VLSMs could be extracted using snapshot POD, by restricting our attention to the streamwise velocity component. Figure 11(a) shows the first reconstructed POD mode in the upstream flow, while figure 11(b) shows the first POD mode $5D$ downstream the bend. It can be seen that the azimuthal frequency is reduced and the streamwise frequency is increased. It is, however, important to recognize that the second mode downstream is nearly identical to the first one upstream, which indicates that the change of the VLSMs is slight.

CONCLUSION

In pipe flow, the presence of a bend may be noticed as far upstream as $10D$ upstream. This is indicated by a small deviation in the axial velocity profile from the fully-developed profile, and the velocity profile is no longer axisymmetric. The deviation is amplified as the flow passes through the bend, and immediately after the bend the velocity profile is skewed towards the outside of the bend, as expected, and the profile also loses its circular appearance and is flattened out along the pipe wall. The mean flow field is slow to recover, taking more than

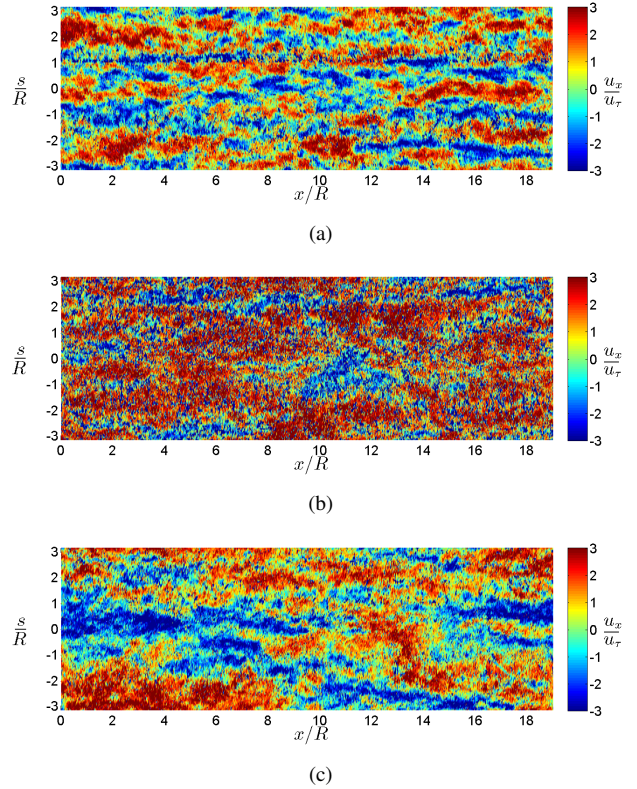


Figure 8. Contour plots of the streamwise velocity fluctuations at $(1 - y/R) = 0.2$, constructed using Taylor's hypothesis. (a) Instantaneous fluctuations in fully developed pipe-flow upstream of the bend at $Re_D = 12,500$, (Hellström et al. 2011); (b) Instantaneous fluctuations $5D$ downstream a 90° bend at $Re_D = 12,500$; (c) Instantaneous fluctuations $5D$ downstream a 90° bend at $Re_D = 16,000$. Flow is from left to right.

20 but less than $50D$ downstream of the bend.

It has been shown that the Dean motions are weak, and that they coexist with a large scale swirling motion, also induced by the pipe curvature, that seems to randomly switch its direction of rotation. The swirling motion does not show up in the mean flow since it is canceled out over long averaging-

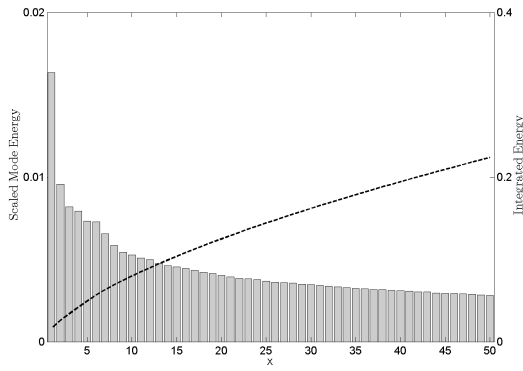


Figure 9. The scaled energy content of the first 50 POD modes, using all three velocity components. The integrated energy is shown by the dashed line.

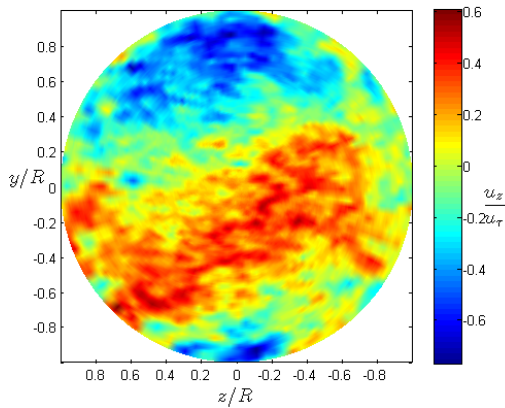


Figure 10. The first mode for all three components visualized by a contour plot of the scaled horizontal velocity component for $Re_D = 12,500$. The outer curvature is to the left and inner to right. The first mode shows the two cell Dean motion, which is the most energetic motion at downstream position $5D$.

ing times, and therefore is only revealed using instantaneous data. However, even though the Dean motion is far from the strongest vorticity structure, it corresponds to the most energetic POD mode in the downstream region. The Dean motion together with the swirl modes constitute the first five POD modes. It was also shown that the VLSMs persist after the bend, but they are no longer the most energetic motion, as they were in the upstream flow. They may be extracted by considering only the streamwise velocity component. The VLSMs seems to be largely unaffected by the secondary motions induced by the pipe curvature, although their shape seems to be slightly wider and shorter.

We are grateful for the financial support received under AFOSR Grant FA9550-09-1-0569 (Program Manager John Schmisser) and ONR Grant N00014-09-1-0263 (Program

Manager Ron Joslin).

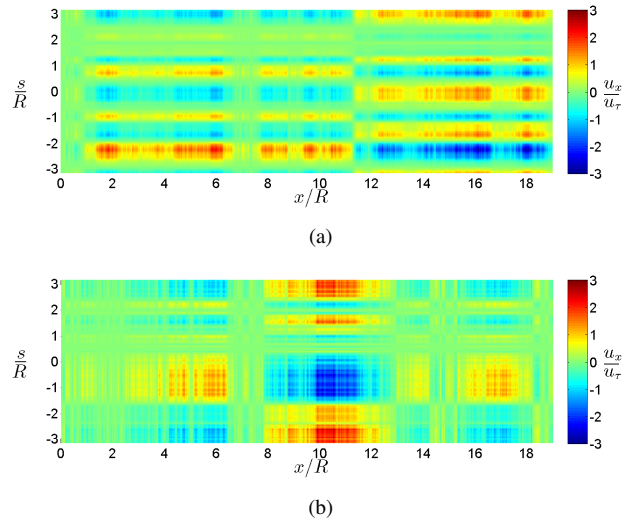


Figure 11. Contour plots of the streamwise velocity fluctuations at $(1 - r/R) = 0.2$ and $Re_D = 12,500$, constructed using Taylor's hypothesis. (a), Mode 1 upstream (Hellström et al. (2011)); (b) Mode 1 $5D$ downstream the 90° bend. Flow is from left to right.

REFERENCES

- Bailey, S. C. C. and Smits, A. J. 2010 Experimental investigation of the structure of large- and very large-scale motions in turbulent pipe flow. *J. Fluid Mech.* **651**, 339–356.
- Balakumar, B. J. and Adrian, R. J. 2007 Large- and very-large-scale motions in channel and boundary-layer flows. *Phil. Trans. R. Soc. A* **365**, 665–681.
- Berger, S. A., Talbot, L. and Yao, L.-S. 1983. Flow in curved pipes. *Ann. Rev. Fluid Mech.* **15**, 46–512.
- Boiron, O., DelPlano, V. and Pelissier, R. 2007 Experimental and numerical studies on the starting effect on the secondary flow in a bend. *J. Fluid Mech.* **574**, 109–129.
- van Doorne, C. W. H. and Westerweel, J. 2007 Measurement of laminar, transitional and turbulent pipe flow using Stereoscopic-PIV. *Exp. Fluids* **42**, 259–279.
- Harlock, J. H. 1955 Some experiments on the secondary flow in a pipe. *Proc. R. Soc. London* **234** 335–346.
- Hellström, L. H.O., Sinha, A. and Smits, A. J. 2011 Visualizing the very-large-scale motions in turbulent pipe flow. *Phys. Fluids* . **23**, 011703.
- McKeon, B. J., Zagarola, M. V. and Smits, A. J. 2005 A new friction factor relationship for fully developed pipe flow. *J. Fluid Mech.* . **538**, 429–443.
- McKeon, B. J. and Sharma, A. S. 2010 A critical layer framework for turbulent pipe flow. *J. Fluid Mech.* . **658**, 336–382.
- Monty, J. P., Stewart, J. A., Williams, R. C. and Chong, M. S. 2007 Large-scale features in turbulent pipe and channel flows. *J. Fluid Mech.* **589**, 147–156.
- Sudo, K., Simuda M. and Hibara H. 1998 Experimental investigation on turbulent flow in a circular sectioned bend. *Experiments in Fluids* **25** 42–49.
- Tunstall, M. J. and J. K. Harvey, J. K. 1968 On the effect of a sharp bend in a fully developed turbulent pipe-flow *J. Fluid Mech.* **34**, 595–608.